RESEARCH ARTICLE

Energy & Environmental Materials WILEY

Supercapacitor

Room Temperature Synthesis of Vertically Aligned Amorphous Ultrathin NiCo-LDH Nanosheets Bifunctional Flexible Supercapacitor Electrodes

*Kwadwo Asare Owusu, Zhaoyang Wang, Ali Saad, Felix Ofori Boakye, Muhammad Asim Mushtaq, Muhammad Tahir, Ghulam Yasin, Dongqing Liu, Zhengchun Peng, and Xingke Cai**

Developing a simple scalable method to fabricate electrodes with high capacity and wide voltage range is desired for the real use of electrochemical supercapacitors. Herein, we synthesized amorphous NiCo-LDH nanosheets vertically aligned on activated carbon cloth substrate, which was in situ transformed from Co-metal–organic framework materials nano-columns by a simple ion exchange process at room temperature. Due to the amorphous and vertically aligned ultrathin structure of NiCo-LDH, the NiCo-LDH/activated carbon cloth composites present high areal capacities of 3770 and 1480 mF cm^{-2} as cathode and anode at 2 mA cm^{-2}, and 79.5% and 80% capacity have been preserved at 50 mA cm^{-2}. In the meantime, they all showed excellent cycling performance with negligible change after >10 000 cycles. By fabricating them into an asymmetric supercapacitor, the device achieves high energy densities (5.61 mWh cm^{-2} and 0.352 mW cm^{-3}). This work provides an innovative strategy for simplifying the design of supercapacitors as well as providing a new understanding of improving the rate capabilities/cycling stability of NiCo-LDH materials.

1. Introduction

Highly efficient energy storage devices are indispensable for the next breakthrough technologies, such as autonomous and unmanned aerial vehicles, 5G, and Internet of Things "smart" devices.[1–3] Presently, the energy storage market niche is dominated by lithium-ion batteries (LIBs) due to their remarkable energy densities.[4–7] Nonetheless, serious challenges, surrounding the limited reserves of lithium resources and the safety issue of LIBs, have opened an avenue for the exploration of other low-cost and greener energy storage devices. A particular device with great prospects for fast-charging, long-lasting storage is the supercapacitor (SC).[8–11] This is due to its fast uptake and release of energy as well as long-cycling properties. However, in comparison with LIBs, its energy density is much lower, restricting its wide utilization.

Several strategies have been devised over the years to increase the energy densities of electrochemical capacitors (ECs), notably designing asymmetric SCs.[9,12–14] The asymmetric SC (ASC) is endowed with cell voltages beyond 1.23 V from the smart matching of different pseudocapacitive cathodes, such as Na_xMnO_2, and anode materials, such as FeOOH, with different stability potentials in a single device, leading to higher energy densities.[15,16] Despite the extensive studies, innovative electrode designs with a focus on functionality and ease of synthesis are still required to further advance ASC research.

Developing a freestanding bifunctional SC electrode with good stability in different positive and negative voltage windows would not only simplify the construction of SC devices but also enhance the energy/power density of the fabricated device because of the wide voltage. Transition metal-based layered double hydroxides (LDHs), which show high capacity as SC electrodes, are highly attractive for this application owing to their fully exposed active sites and high electrochemical activity.[17–19] However, despite the high theoretical capacity of crystalline LDHs, they still present inferior rate capabilities and poor cycling performance. Mostly, the LDHs are only used as cathodes. On the other hand, carbon materials have been demonstrated to be a good SC anode with good electrical conductivity. Therefore, the hybrids of LDHs and carbon materials should be good bifunctional materials for SCs but need

Dr. K. A. Owusu, Dr. A. Saad, Dr. M. A. Mushtaq, Dr. G. Yasin, Prof. X. Cai
Institute for Advanced Study, Shenzhen University, Shenzhen 518060, China
E-mail: cai.xingke@szu.edu.cn
Dr. K. A. Owusu, Dr. A. Saad, Dr. Ghulam Yasin, Prof. Z. Peng
College of Physics and Optoelectronics, Shenzhen University, 3688 Nanhai Boulevard, Nanshan District, Shenzhen 518060, China
Dr. Z. Wang
School of Chemistry and Materials Science, Hubei Engineering University, No. 272 Traffic Avenue, Xiaogan 432000, China
Dr. Z. Wang, Dr. F. O. Boakye
State Key Laboratory of Advanced Technology for Materials Synthesis and Processing, Wuhan University of Technology, No. 122 Luoshi Road, Wuhan 430070, China
Dr. M. Tahir
Key Laboratory of Green Printing, CAS Research Centre for Excellence in Molecular Science, Institute of Chemistry Chinese Academy of Sciences (ICCAS), Beijing 100190, China
Dr. D. Liu
College of Mechatronics and Control Engineering, Shenzhen University, 3688 Nanhai Boulevard, Nanshan District, Shenzhen 518050, China
The ORCID identification number(s) for the author(s) of this article can be found under https://doi.org/10.1002/eem2.12545.

DOI: 10.1002/eem2.12545

experimental evidence. In the meantime, the good conductivity of carbon materials should also help the charge transfer at the electrode/electrolyte interfaces.

In our previous work, we successfully demonstrated a capacitive dominant charge storage mechanism in low-crystalline iron hydroxides, resulting in stable cycling performances and exceptional rate capabilities over their crystalline counterpart.[14] The preparation of amorphous hydroxides has been reported in other complicated procedures, which also showed decent performance as SC electrodes.[20] However, the preparation of low crystalline or amorphous LDH with exceptional electrochemical performance has been overlooked in previous research. In the meantime, a facile preparation method for scalable production of low-crystalline/amorphous hydroxides on the conductive carbon substrates is still lacking. Thanks to their unique shape and particle sizes, modulation of metal–organic framework materials (MOFs) serves as an effective strategy for developing high-performance SC electrodes including metal oxides, sulfides, and nitrides.[21–23]

In this work, we developed a method to transform the Co-based MOF precursors into amorphous structured LDH with vertically aligned ultrathin sheet morphology on activated carbon cloth (ACC) substrates. This transformation was based on an ion exchange mechanism between the MOFs and metal ions in the ethylene glycol/water mixed solution. This method should also be suitable to prepare various Co-containing amorphous LDH nanosheets. The amorphous NiCo-LDH vertically aligned nanosheets on ACC (NiCo-LDH/ACC) has been used as a bifunctional electrode for the cathode and anode in KOH electrolyte. It presents a high area capacitance of 3770 mF cm^{-2} at 1 mA cm^{-2}, rate capability of 79.5% at 50 mA cm^{-2}, and cycling stability of 88% after 5000 cycles as a cathode. An area capacitance of 1480 mF cm^{-2}, rate capability of 80% at 50 mA cm^{-2}, and stable cycling of up to 10 000 cycles were achieved for the anodic performance. The full device also presents both high energy and power density, ranking it among the best values for LDH-based SC electrodes.

2. Results and Discussions

The NiCo LDH interconnected nanosheets on ACCs were synthesized using a facile room-temperature method as illustrated in **Figure 1**.

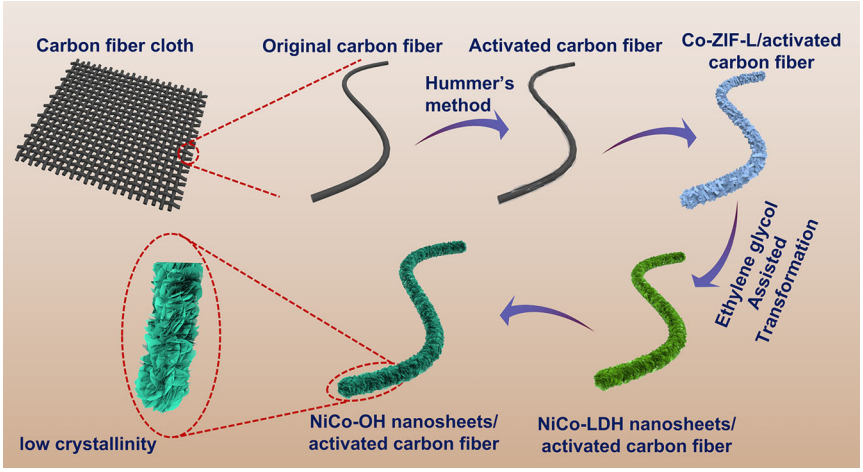

Figure 1. Representative schematic for the room temperature synthesis of NiCo-LDH/ACC bifunctional electrode.

Firstly, a modified Hummer's method was employed to activate the surface of carbon cloths, generating exfoliated carbon sheets on their surface. This activation process for the carbon cloth is necessary, which can not only make the surface hydrophilic but also bring oxidative functions to them. The hydrophilicity can help the growth of Co-ZIF-L on the ACC. Moreover, the oxidative functional groups accelerate the oxidation of Co^{2+} to Co^{3+} to form NiCo-LDH. Then, Co-MOF was grown on the surface of ACC in a water solution containing Co^{2+} and 2-methylimidazole (2-MEIM). Afterward, the Co-MOF decorated ACC was transformed into NiCo-LDH through an ethylene glycol-assisted sequential transformation in a Ni/Co salt mixed solution. The final NiCo LDH/ACC was dried in argon gas at a low temperature. The X-ray diffraction (XRD) pattern of the Co-MOF material grown on the ACC fully matches the simulated XRD pattern of Co-ZIF-L crystals (**Figure 2**a and Figure S1, Supporting Information).[24,25] The transformation from Co-MOF to NiCo-LDH nanosheets is confirmed from the XRD pattern (JCPDS No. 33-0429).[26–29] Specifically, the XRD pattern of both NiCo-LDH/ACC nanosheets and NiCo-LDH powder reveal weak peaks at 11.6°, 34.4°, and 60.5°, which can be indexed to (003), (012), and (110), respectively.[28,29] The characteristic peaks of the carbon fiber cloths substrate are positioned at 25.2° and 43.8°, respectively.[30]

Then, X-ray photoelectron spectroscopy (XPS) was utilized to understand the chemical states of the synthesized NiCo-LDH material. The full survey spectrum for NiCo-LDH/ACC presents a ratio of 1:1.15 for Ni/Co, which is similar to the NiCo-LDH powdery sample (Figures S2a and S3a, Supporting Information).[31] The deconvoluted Co 2p high-resolution spectrum displayed in Figure 2b exhibits two spin-orbit peaks, Co $2p_{3/2}$ and Co $2p_{1/2}$ with binding energies of 779.4 and 795 eV, as well as their corresponding satellite peaks. Further analysis of the XPS peaks of the deconvoluted Co $2p_{3/2}$ and Co $2p_{1/2}$ peaks reveal the coexistence of Co^{2+} (796.4 and 781.3 eV) and Co^{3+} (794.5 and 779.5 eV), which is also similar with the NiCo-LDH powdery materials (Figure S3b,c, Supporting Information), confirming the successful synthesis of NiCo-LDH on the ACC.[32–34]

The presence of functional groups on the surface of ACC will also encourage the transformation of Co-ZIF-L into NiCo-LDH by accelerating the oxidation of Co^{2+} to Co^{3+} as reported in previous research.[35,36] The deconvolution of the Ni $2p_{3/2}$ spectrum also presents two major peaks with binding energies of 856.4 and 853.8 eV, indicating the presence of Ni^{2+} and Ni^{3+} in the sample (Figure 2c).[37,38] The deconvoluted O 1s spectrum presents three distinct peaks (Figure S2b, Supporting Information and **Figure 3**d) with binding energies of 529.1, 530.7, and 531.5 eV, respectively, which are ascribed to the metal-oxygen bonds (Ni–O, Co–O), hydroxyl bonds (OH) from NiCo-LDH and absorbed oxygen on the surface of NiCo-LDH materials.[39] The structure of the NiCo-LDH nanosheets was also characterized by Raman spectroscopy (Figure 2d). The Raman peaks positioned at 459 and 521 cm^{-1} correspond to the metal–oxygen–metal (M–O–M) bonds while the peak positioned at 1042 cm^{-1} is attributed to the insertion of CO_3^{2-} in the interlayers of NiCo-LDH.[27] These characters fully confirm the transformation of Co-ZIF-L to NiCo-LDH. All these initial structural characterizations indicate

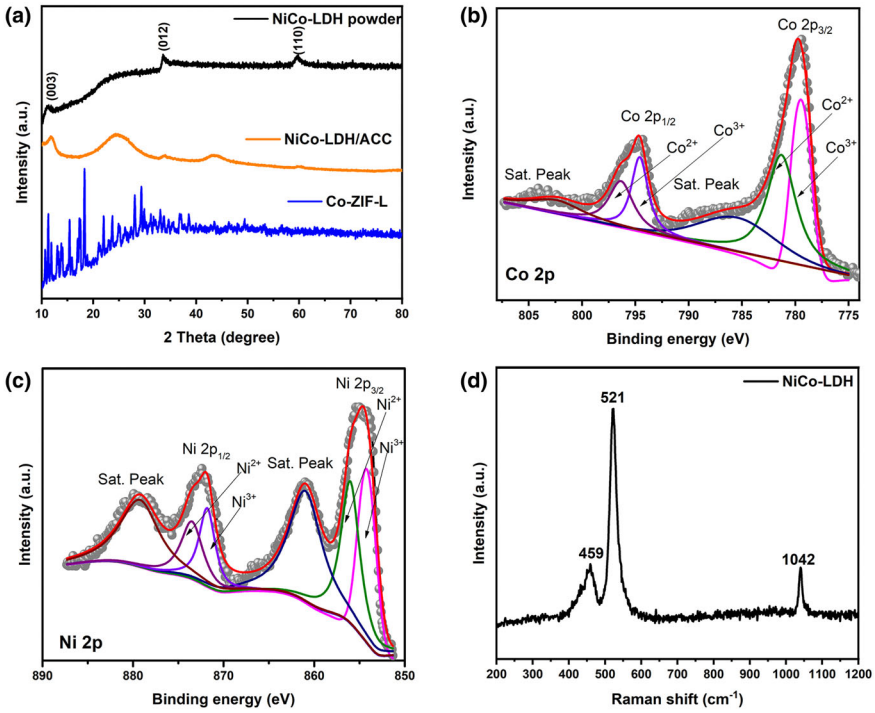

Figure 2. a) XRD patterns of Co-ZIF-L, NiCo-LDH powder, and NiCo-LDH/ACC. XPS spectra of b) Co 2p and c) Ni 2p of NiCo-LDH nanosheets on activated carbon cloth substrate, and d) Raman spectrum of NiCo-LDH.

that NiCo-LDH materials with low crystallinity have been prepared on the surface of ACC.

The morphological evolution from Co-ZIF-L square columns to NiCo-LDH interconnected nanosheets was carefully studied using scanning and transmission electron microscopy (SEM and TEM). Primarily, carbon cloths possess a smooth surface (Figure S4, Supporting Information). After activation, the SEM image of the ACC reveals exfoliated carbon sheets on the surface of carbon cloths (Figure 3a). The thin carbon sheets connected with ACC would enhance its surface wettability, which is beneficial for the growth of Co-MOF material. From Figure 3b, the Co-MOF on the ACC showed a square column-like morphology with a genuine width/length of 250 nm/1 μm. These columns were converted into 3D LDH nanosheets on the surface of ACC, as illustrated in Figure 3c. From the SEM image, the NiCo-LDH nanosheets have an ultrasmall thickness but are connected into a 3D mesoporous structure strongly attached to the surface of ACC. The NiCo-LDH/ACC displays a type-IV isotherm with a hysteresis loop, which is a typical characteristic of mesoporous materials (Figure S5a, Supporting Information). The average pore diameter is 3.9 nm. The Brunauer–Emmett–Teller surface area of NiCo-LDH/ACC is determined to be 25.8 m^2/g, much larger than the Co-MOF/ACC (2.4 m^2/g), indicating the conversion of Co-MOF into NiCo-LDH nanosheets has greatly increased the surface area of the sample. The high surface area and mesoporous features of the NiCo-LDH material will generate numerous active sites for charge storage and easy accessibility to electrolyte ions, greatly benefiting the SC performances.[40]

Then, TEM analysis was employed to gather information on the microstructures of the as-formed LDH nanosheets. The low-magnification TEM image reveals that the 3D NiCo-LDH material is composed of several ultrathin nanosheets strongly interconnected together (Figure 3d, e). A high-resolution TEM (HRTEM) image (Figure 3f) indicates the existence of abundant nanopores on the thin nanosheets, presenting a large electroactive surface area for charge storage. In the meantime, the HRTEM image does not exhibit noticeable lattice fringes, indicating the amorphous structure of as-synthesized material (Figure 3g). The dull selected area electron diffraction (SAED) pattern reveals rings (Figure 3h) corresponding to the (110), (012), and (015) planes of NiCo-LDH, respectively. This is due to the transformation of Co-ZIF-L to low-crystalline/amorphous NiCo-LDH. These results are highly consistent with the XRD results, where only broad peaks for NiCo-LDH exist. The high-angle annular dark field (HAADF) image and energy dispersive spectroscopic (EDS) mapping indicates the uniform distribution of nickel (Ni), cobalt (Co), and oxygen (O) elements in the NiCo-LDH material (Figure 3i). It means the reaction between the Co-MOF square columns and the Co^{2+}/Ni^{2+} containing ethylene glycol solution was genuine, but the crystal structure cannot be formed due to the insufficient reaction thermodynamics at room temperature.

To understand the mechanism to form amorphous NiCo-LDH, the Co-MOF/ACCs were put into different solutions to see the transformation process at room temperature. Previous work reported the transformation of MOFs into LDH in transition metal salts dissolved in ethanol or methanol. The hydrolysis of metal ions with the solvent produces H^+, which will gradually etch the MOFs and the dissolved metal ions will reform into LDH materials on the surface of the MOFs.[41,42] As time continues, the MOFs will totally transform into LDHs. In our case (Figure S6 and Table S1, Supporting Information), we found the Co-MOF film on the ACCs was totally removed in the pure ethylene glycol solution. However, they were transformed into green-colored NiCo-LDH in both water and ethylene glycol/water mixed solvents. The NiCo-LDHs formed in both solvents show much poorer crystallinity than the ones formed in the typical ethanol or methanol solvent.[41,43] The mechanism for such difference should be ascribed to the different formation energy of the LDHs in a different solvent, where the crystallization of LDHs in water is more difficult than in the ethanol and methanol.[43,44] With the help of viscous ethylene glycol, the recrystallization becomes even more difficult, forming the amorphous structure.

Previous works indicate that amorphous materials show better electrochemical performances than their crystalline counterparts due to the more exposed active sites.[45] In the meantime, the ultrathin interconnected NiCo-LDH was vertically aligned on the ACCs, which provides easy access of the ions to the LDH surface and good charge transfer at the electrode/electrolyte interface. All these structural and morphologic characters indicate the NiCo-LDH/ACC materials are good candidates for SC applications. It is expected to be a promising bifunctional electrode material as cathode and anode for SCs, owing to the integration of NiCo-LDH and ACC in a single electrode.

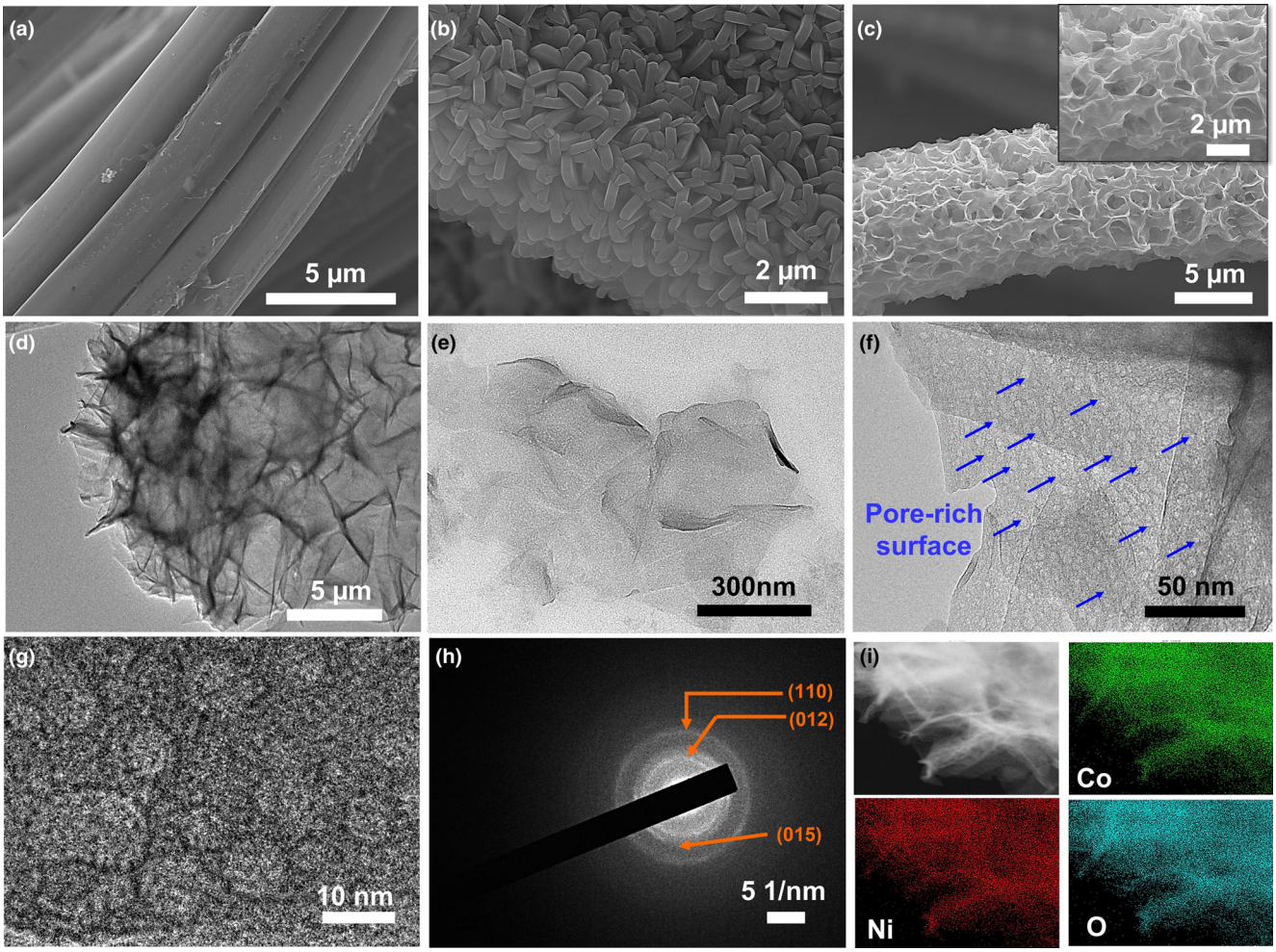

Figure 3. a) SEM image of the activated CC. b) SEM image of Co-MOF grown on the activated CC. c) SEM image of the NiCo-LDH/ACC nanonetwork structure (inset: high magnification SEM image of the NiCo-LDH). d) TEM image of the NiCo-LDH nanonetwork nanosheets at low magnification. e) TEM image of the NiCo-LDH nanosheets obtained at high magnification. f) HRTEM image of the NiCo-LDH nanosheets illustrating porous structure. g) HRTEM image of the NiCo-LDH nanosheets illustrating amorphous structure. h) Selected area electron diffraction (SAED) analysis of the NiCo-LDH nanosheets. i) High-angle annular dark field (HAADF) images depicting the presence of nickel, oxygen, and cobalt elements in the obtained structure.

To confirm this speculation, its performance as a potential cathode material for hybrid SCs was firstly checked in a three-electrode system. Platinum (Pt) foil and saturated calomel electrode (SCE) were used as the counter and reference electrodes, respectively, while NiCo-LDH/ACC with a size of 1 cm^2 was used as the free-standing working electrode. The cyclic voltammetry (CV) curves were tested between 1 and 10 mV s^{-1} (**Figure 4a**). The curves show a pair of broad reversible redox peaks, which are assigned to the following reversible reactions of Ni/Co ions between 2+ and 3+:[27,46–49]

$$Ni(OH)_2 + OH^- \leftrightarrow NiOOH + e^- + H_2O \quad (1)$$

$$Co(OH)_2 + OH^- \leftrightarrow CoOOH + e^- + H_2O \quad (2)$$

$$CoOOH + OH^- \leftrightarrow CoO_2 + e^- + H_2O \quad (3)$$

The symmetric redox profile of the synthesized material is still maintained with the increase of the scan rate up to 10 mV s^{-1}, suggesting good reversibility and superior storage capability. All the curves showed a broad redox platform, suggesting a substantial contribution of the capacitance from the battery-type Faradic storage mechanism. The NiCo-LDH exhibits a similar symmetric redox profile in 1 M and 3 M KOH electrolytes at both low and high scan rates, respectively (Figure S7, Supporting Information). The platform around 0.3 V in the galvanostatic charge/discharge curves of the NiCo-LDH/ACC also demonstrated the big contribution of the pseudocapacitance for the whole capacity (Figure S8, Supporting Information). The capacity storage mechanism can be analyzed by the following equation:

$$i(v) = av^b, \quad (4)$$

where i is the current density for the peaks, v is the scan rate, and a and b are constants. A b-value of 0.5 denotes an ion diffusion-controlled reaction process, while a b-value of 1 indicates a capacity-controlled process.[50] The as-obtained b values for the oxidation and reduction peaks of the NiCo-LDH/ACC electrode are

0.633 and 0.629, respectively (Figure S9, Supporting Information), indicating a blend of capacity- and diffusion-controlled storage mechanism in the NiCo-LDH/ACC. Then, the capacity was quantitatively separated into capacitive and diffusion-controlled contributions using the equation:

$$i(v) = k_1 v + k_2 v^{\frac{1}{2}}, \quad (5)$$

where $k_1 v$ and $k_2 v^{\frac{1}{2}}$ stand for diffusion- and capacity-controlled processes, respectively. From the pseudo-capacitive analysis based on the representative CV curve (Figure 4b), the capacity- and diffusion-controlled capacitances can be quantitatively separated. The capacitive contribution is determined to be 60.1%, 71.6%, 87.2%, and 95.4% at 1, 2, 5, and 10 mV s^{-1}, respectively (Figure S10, Supporting Information), which clearly demonstrated the capacity are contributed both by the surface area related double layer capacitance and the surface redox reaction related pseudo-capacitance. The shift in potential and larger pseudocapacitive responses than the overall current responses are due to an unaccounted ohmic drop. The areal capacitances at each current density were calculated from the galvanostatic discharge curves. The NiCo-LDH/ACC electrode presents a high areal capacitance of 3770 mF cm^{-2} at 1 mA cm^{-2} (Figure 4c). The gravimetric capacitance based on the weight of NiCo-LDH alone (~2 mg cm^{-2}) and the whole electrode (~13 mg cm^{-2}) were calculated as well with values of 1887 and 290 F g^{-1} at 1 mA cm^{-2}, respectively (Figure S11, Supporting Information). Both the areal and gravimetric capacitance values at low current density (1 mA cm^{-2}) are higher than the literature-reported data for NiCo-LDH-based cathodes (Table S2, Supporting Information).[25,34,51–63] At 1 mV s^{-1}, the double-layer capacitance contribution was 40% and the pseudo-capacitance contribution was 60%. The double-layer capacitance is related to the surface area and pseudo-capacitance is mainly related to the population of active metal ions on the surface. Their ultrathin structure and high-density nanopores on their surfaces should be the reason for the large double-layer capacitance. The amorphous structure of the ultrathin sheets contributes to the large pseudo-capacitance, which provides more Ni/Co sites toward the redox reaction with OH^-. A high areal capacity of 3000 mF cm^{-2} is still retained after increasing the current density to 50 mA cm^{-2}, that is, 79.5% of the capacitance being reserved, which is superior to most reported NiCo-LDH-based cathode (Table S2, Supporting Information). The rate performance is influenced by the accessibility of the OH^- ions in the solution to the Ni/Co ions on the surface and the charge transfer at the electrode/electrolyte interface. The good rate performance for NiCo-LDH/ACC can be ascribed to the vertically aligned and interconnected structure of NiCo-LDH on the conductive ACCs, which can facilitate the access of hydroxide ions (OH^-) to the Ni/Co-active sites and the charge transfer at the electrolyte/electrode interface.

The NiCo-LDH/ACC electrode also exhibits good cycling performance with capacitance retention of 88% after 5000 cycles (Figure 4d). The good cycling performance can be ascribed to the amorphous structure of the active NiCo-LDH nanosheets, which show better stability than crystalline NiCo-LDH sheets.[14,20,64] Electrochemical impedance spectroscopy (EIS) analysis was employed before and after stability tests to understand the change of kinetics during the cycling process (Figure 4e). The bulk resistance (R_s) is the inherent resistance of the electrode material, ionic resistance of the electrolyte, and the contact resistance at the interface between electrolyte and electrode, while the

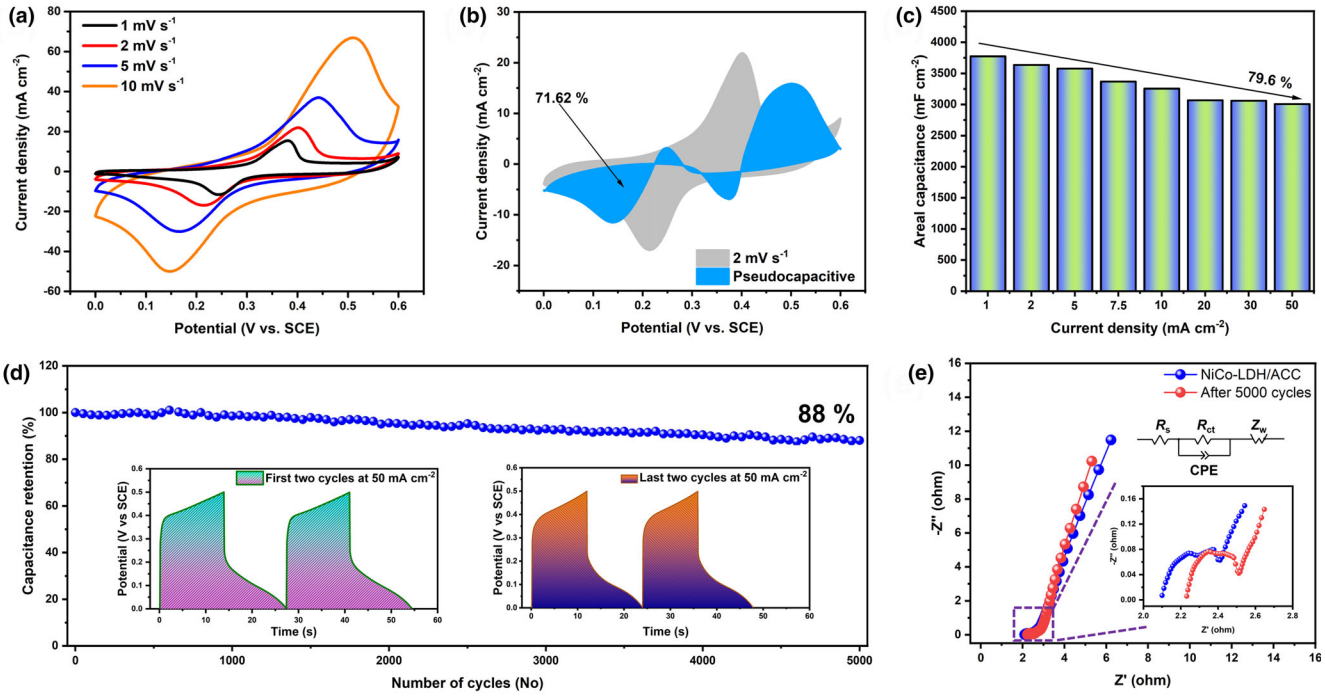

Figure 4. a) Cyclic voltammetry curves of NiCo-LDH/ACC between 1 and 10 mV s^{-1}. b) Capacity separation analysis at 2 mV s^{-1}. c) Areal capacitance of the NiCo-LDH/ACC at different current densities. d) Cycling performance of the NiCo-LDH/ACC electrode at 50 mA cm^{-2}. e) Nyquist plots of NiCo-LDH/ACC before and after cycling (inset: high-frequency region of the EIS curve).

charge transfer resistance (R_{ct}) is the resistance against the process of the electron transfer at the electrode/electrolyte interface.[65] The NiCo-LDH presents an R_s of 2.1 Ω and an R_{ct} of 0.22 Ω (Table S3, Supporting Information). After 5000 cycles, the R_s and R_{ct} are 2.24 and 0.21 Ω, indicating the good stability of the electrode during the cycling process (Figure 4e, inset). Therefore, the NiCo-LDH/ACC cathode presents superior comprehensive performance, including exceptional areal/gravimetric capacitances, good rate performance, and long cycling life, due to its unique morphology and structure formed during the room temperature transformation process.

The anodic performance of NiCo-LDH/ACC for SCs have been studied between −0.1 and −1.2 V (vs SCE). The CV curves for ACC and NiCo-LDH/ACC anode at 5 mV s^{-1} (**Figure 5a**) clearly indicate the NiCo-LDH/ACC shows a larger capacitance due to the growth of NiCo-LDH on ACC. Typical CV curves of NiCo-LDH/ACC measured at different scan rates (5–50 mV s^{-1}), demonstrating a main capacitive behavior with no apparent redox peaks (Figure 5b). Their areal capacitances were calculated from the galvanostatic charge/discharge curves at different current densities. Typically, the NiCo-LDH/ACC presents a longer discharge time than ACC (Figure 5c), which indicates the larger area capacitance for the NiCo-LDH/ACC than ACC. As displayed in Figure 5d, the NiCo-LDH/ACC presents an areal capacitance of 1480 mF cm^{-2} at 1 mA cm^{-2}, much higher than the ACC (1120 mF cm^{-2}). With the increase of the current density to 50 mA cm^{-2}, the NiCo-LDH/ACC maintains an areal capacitance of 1190 mF cm^{-2}, corresponding to 80% retention compared with the capacitance at 1 mA cm^{-2}. The cycling performance of the NiCo-LDH/ACC anode was tested at 50 mA cm^{-2} (Figure 5e), showing 100% capacitance retention even after 10 000 cycles. All these results indicate that NiCo-LDH/ACC is a better anode material than the pure ACC due to the large surface area of the NiCo-LDH on the surface and its good contact with the ACC. The excellent performance of the NiCo-LDH/ACC anode over the ACC anode can be attributed to the increased surface area of the ACC after the growth of vertically NiCo-LDH nanosheets and the unrestrained fast charge transfer in the designed anode.

Lastly, a full symmetric SC device was fabricated by applying the NiCo-LDH/ACC as cathode and anode (**Figure 6a**). First, CV analysis was done in incremental potential ranges to determine the optimum cell voltage for the full device (Figure S12, Supporting Information). The obtained data clearly illustrates that the NiCo-LDH/ACC electrode is stable up to 1.7 V without any contribution from water splitting. Next, CV curves were tested at scan rates from 5 to 50 mV s^{-1} in the 0–1.7 V voltage range (Figure 6b). The CV curves exhibit broad reversible peaks at both low and high scan rates, signifying the big contribution from the pseudo-capacitance. Charge separation analysis was further carried out to quantitively analyze the capacity contributions from the capacity-controlled process and diffusion-controlled process (Figure 6c). When the scanning rate increases from 5 to 50 mV s^{-1}, the capacitive contribution for the 1.7 V device increases from 52.2% to 81.1% (Figure S13, Supporting Information). The galvanostatic charge/discharge curves for the device exhibit somewhat linear curves without obvious potential platforms, indicating a mixed storage mechanism from both double-layer capacitance and redox reaction-based pseudo-capacitance (Figure 6d). The fabricated device realizes a high areal capacitance of 876 mF cm^{-2} at 2 mA cm^{-2} (Figure 6e). An area capacitance of 576 mF cm^{-2} is still retained at 35 mA cm^{-2}, realizing a rate capability of 66.4%. The areal and volumetric energy and power densities of the fabricated device were calculated from the discharge curves and plotted as Ragone plots.

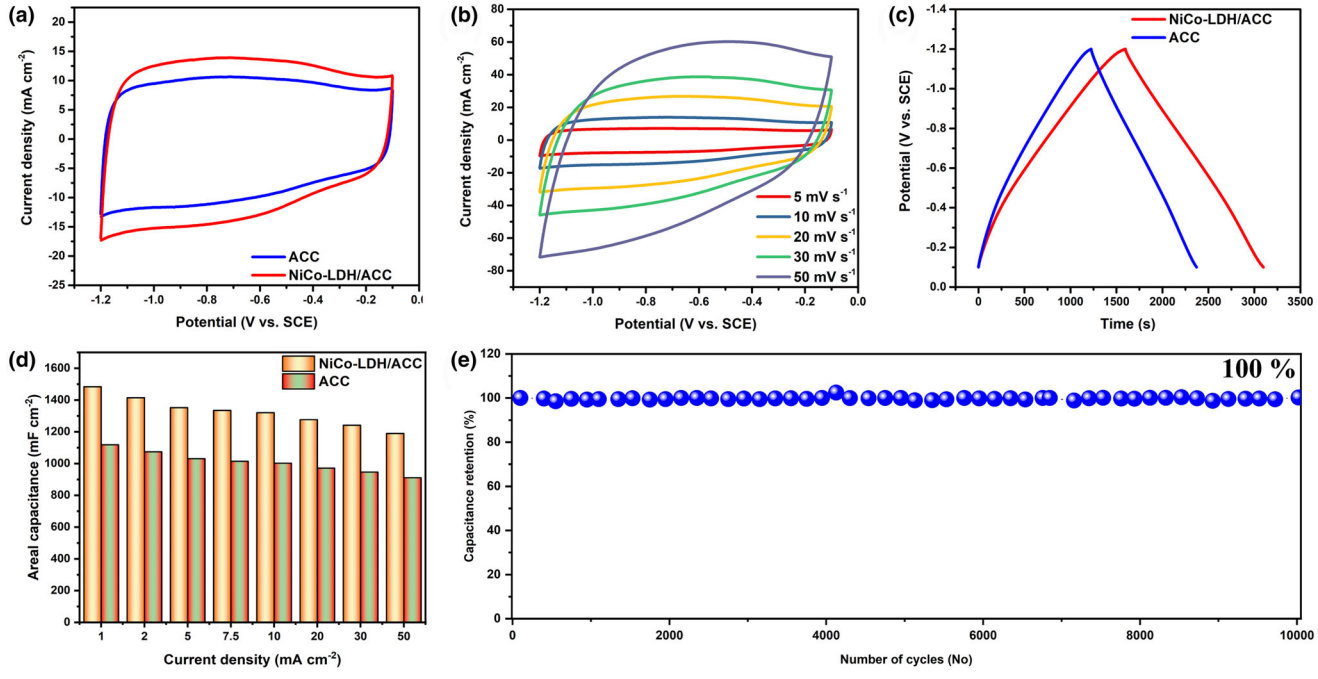

Figure 5. a) Comparison of the CV curves of ACC and NiCo-LDH/ACC electrode at 5 mV s^{-1}. b) CV curves of the NiCo-LDH/ACC between 5 and 50 mV s^{-1}. c) Comparison of the galvanostatic charge–discharge curves of the NiCo-LDH/ACC electrode at 2 mA cm^{-2}. d) Areal capacitance comparison of the NiCo-LDH/ACC and ACC. e) Cycling performance of the NiCo-LDH/ACC electrode at 50 mA cm^{-2}.

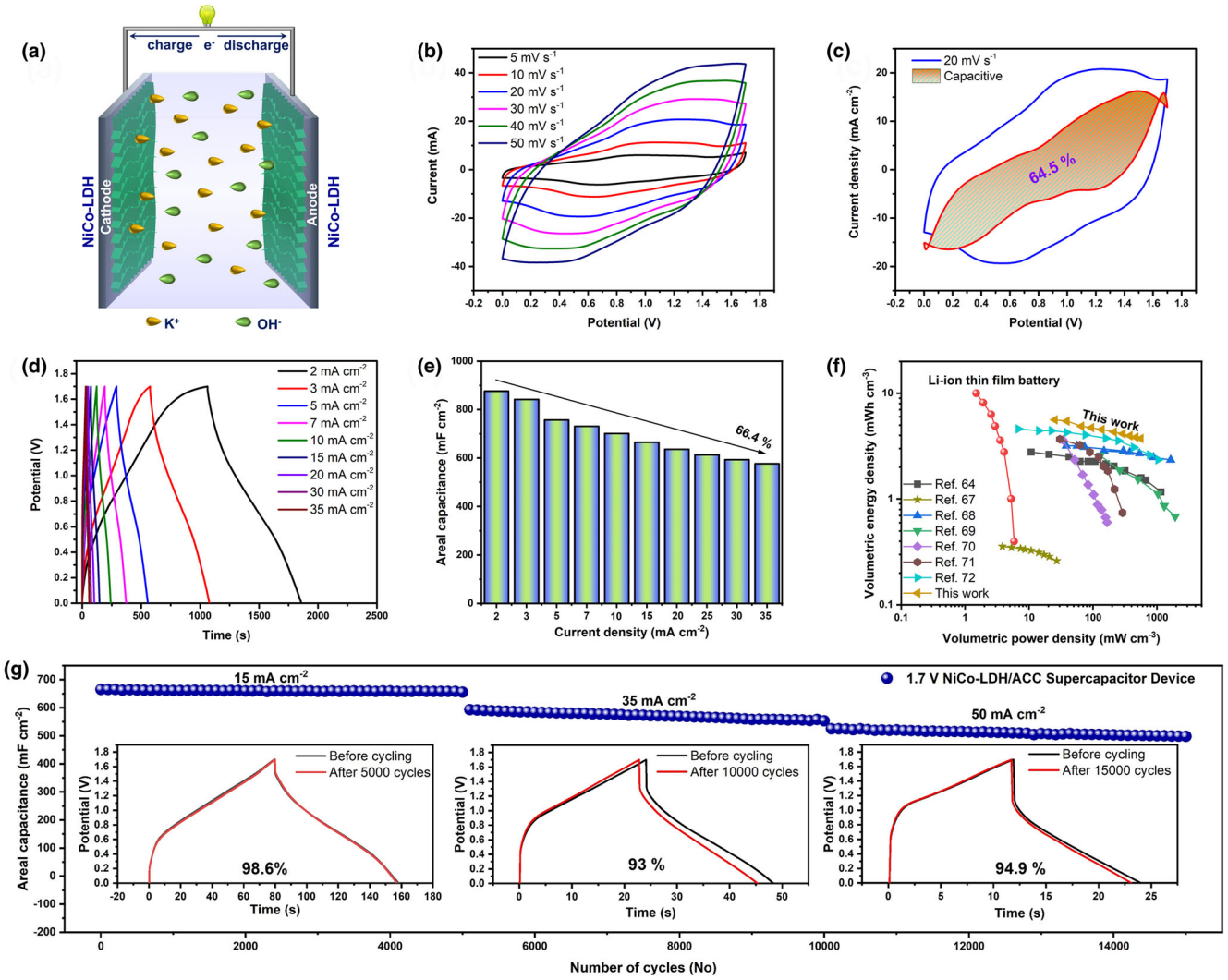

Figure 6. a) Schematic illustration of the NiCo-LDH/ACC symmetric supercapacitor. b) CV curves of the NiCo-LDH/ACC symmetric supercapacitor at different scan rates. c) Charge separation analysis of the 1.7 V NiCo-LDH/ACC symmetric supercapacitor at 20 mV s^{-1}. d) GCD curves of the 1.7 V NiCo-LDH/ACC symmetric supercapacitor device at different current densities. e) Areal capacitance of the 1.7 V NiCo-LDH/ACC symmetric device. f) Ragone plot of the 1.7 V NiCo-LDH/ACC symmetric supercapacitor device. g) Cycling performance of the 1.7 V NiCo-LDH/ACC symmetric supercapacitor device.

As shown in Figure 6f, the fabricated device presents a high volumetric energy density of 5.6 mW h cm^{-3} at a volumetric power density of 25.3 mW cm^{-3} and a maximum volumetric power density of 559.5 mW cm^{-3} at a volumetric energy density of 3.7 mW h cm^{-3}. These values are superior to the volumetric energy and power densities of other reported Co-based aqueous SCs.[63,66–71] In terms of areal energy density, the 1.7 V NiCo-LDH/ACC symmetric device presents a high areal energy density of 0.35 mW h cm^{-2} at a power density of 1.59 mW cm^{-2} and a high-power density of 34.68 mW cm^{-2} at an areal energy density of 0.231 mW h cm^{-2} (Figure S14, Supporting Information). Compared with the conventional NiCo-LDH@carbon devices, the NiCo-LDH/ACC@NiCo-LDH/ACC in this work showed better comprehensive performance (Table S4, Supporting Information). Considering the importance of cycling stability for evaluating the performance of SCs, the cycling performance of the 1.7 V SC device was evaluated at different current densities. As shown in Figure 6g, the symmetric device exhibits long cycling performances over 15 000 cycles with excellent stability at 15, 35, and 50 mA cm^{-2}, respectively.

Electrochemical impedance spectroscopy analysis was used to characterize the mechanism of charge transfer in the symmetric device during charge storage (**Figure 7**). The fabricated device presents a low R_s value of 4.58 Ω and an R_{ct} of 0.43 Ω. An analysis of the Nyquist plot obtained after 15 000 cycles reveals that R_s value is still maintained at 4.58 Ω while the R_{ct} value increases slightly to 0.48 Ω (Figure 7a, inset), confirming the fast diffusion kinetics and low resistances of the electrode during the cycling process (Figure 7a and Table S5, Supporting Information). In the meantime, it means the good stability of the amorphous structured NiCo-LDH nanosheets on the ACC. In summary (Figure 7b), the excellent comprehensive performance of fabricated NiCo-LDH/ACC symmetric SC can be recognized in the following parts:

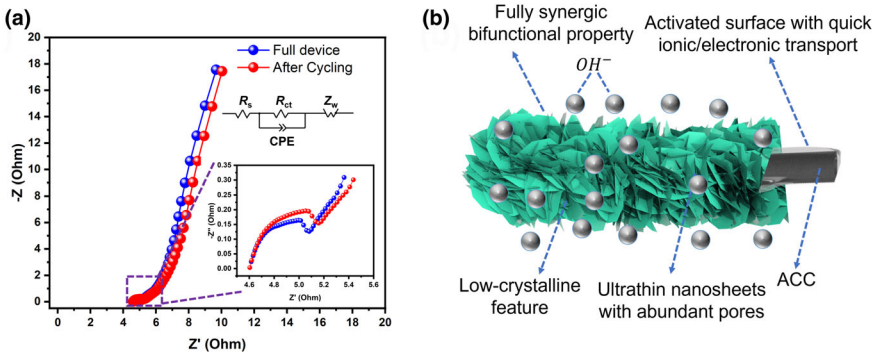

Figure 7. a) Nyquist plot of the 1.7 V NiCo-LDH symmetric supercapacitor before and after cycling (inset: high-frequency region of the EIS curves). b) Schematic illustration of the energy storage mechanism in the NiCo-LDH bifunctional electrode.

1 The bifunctionality as cathode and anode due to the synergistic interaction between the NiCo-LDH and ACC electrode, which can bear high voltage up to 1.7 V.
2 The fast ionic/electronic transport due to the conductive ACC, and the good interface between the ACC and NiCo-LDH.
3 The amorphous NiCo-LDH nanosheets are beneficial for rate and cycling performance.
4 The ultrathin interconnected nanosheet morphology is beneficial for easy electrolyte permeation and faradaic charge storage.

3. Conclusion

An in situ transformation of Co-MOF squares into amorphous LDH nanosheets vertically aligned on ACC has been achieved by dipping the Co-MOF/ACC into a mixed water/ethylene glycol solvent. During the conversion, the ethylene glycol etches the organic ligands of the Co-MOF. The hydrolysis of Ni^{2+} and as-formed Co^{3+} leads to the generation of NiCo-LDH. Due to the large viscosity of ethylene glycol, the diffusion of the metal ions is slow and the crystallization of the LDH is difficult, leading to the formation of an amorphous structure. The as-formed NiCo-LDH/ACC electrode shows excellent performance both as the cathode and anode for SC applications. Using NiCo-LDH/ACC as the cathode, the amorphous structure and the vertically aligned interconnected ultrathin morphology of the NiCo-LDH, lead to a stable capacitance larger than other reported NiCo-LDH materials. The ACC provides good charge transfer during the charging/discharging process, making the NiCo-LDH/ACC electrode show good rate performance at high current densities. Using NiCo-LDH/ACC as the anode, it shows higher capacitance than the ACC due to the increased surface area by the vertically aligned NiCo-LDH on top. In the meantime, the rate performance was similar to the pure ACC. Using the amorphous NiCo-LDH/ACC as both the anode and cathode to fabricate a SC device, it can bear a 1.7 V voltage window without any side reactions. In the meantime, it delivered high volumetric and areal energy density (5.61 mWh cm^{-3} and 0.352 mWh cm^{-2}), high volumetric and areal power density (559.5 mW cm^{-3} and 34.68 mW cm^{-2}), and exceptional cycling performances (stability up to 15 000 cycles with negligible capacity change).

Since the easy preparation and good scalability of the as-prepared flexible electrodes, the method developed in this work may open an avenue for the commercial applications of the high-performance LDH-based SC devices. In the meantime, the method developed in this article should be suitable to prepare various amorphous-structured LDH nanosheets with different metal compositions.

4. Experimental section

Activation of carbon cloths: Carbon cloths were purchased from Shanghai Hesen Co. Ltd and washed sequentially in ethanol, acetone, and water. Then, the pre-treated carbon cloths were soaked in a glass bottle containing 20 mL (98%) H_2SO_4 and 10 mL (70%) HNO_3 for 30 min. Next, 1.5 g potassium permanganate ($KMnO_4$) reagent was slowly introduced into the mixed acidic solution, which was stirred for 10 min. The soaked carbon cloths stand for 12 h at room temperature. Then, 100 mL H_2O was added, and the resultant solution was stirred for 1 h, followed by 3 mL 30% H_2O_2 solution for another hour. Finally, the ACCs were washed several times with deionized water. Finally, they were dried overnight in an oven at 70 °C before being used for subsequent experiments.

Synthesis of Co-MOF on ACCs: A 0.986 g of 2-methylimidazole (2-MEIM) was firstly dissolved in 14 mL water at room temperature. Next, 0.582 g of Co $(NO_3)_2 \cdot 6H_2O$ was dissolved in 2 mL water. The metal salt solution was poured quickly into the 2-MEIM aqueous solution and stirred at room temperature. Next, pieces of prepared ACCs (2 × 5 cm^2) were placed in the precursor solution and aged at room temperature for 6 h. After the aging process, the ACCs covered with a MOF film were removed and gently washed with deionized water to get rid of loosely attached materials. Finally, it was dried overnight in an oven at 70 °C to obtain Co-MOF material.

Synthesis of NiCo-LDH nanosheets on ACCs: The NiCo-LDH on ACCs was synthesized by treating the Co-MOF/ACC with a secondary soaking treatment. In brief, 1:1 $Ni(NO_3)_2 \cdot 6H_2O$ (1 mmol) and $Co(NO_3)_2 \cdot 6H_2O$ were dissolved in water: ethylene glycol mixed solution under a ratio of 2:1 (total volume = 30 mL). Next, the pieces of Co-MOF/ACC were placed in the glass vial and aged for 4 h at room temperature. After that, the electrode with a green film on its surface was washed in deionized water and freeze-dried, which was named NiCo-LDH NSs/ACC. The mass loading of NiCo-LDH on carbon cloth is 2 mg cm^{-2}.

Material characterization: X-ray diffraction measurements were conducted using a Bruker D8 Discover X-ray diffractometer with a Cu Kα X-ray at room temperature as well as a Shimadzu X-ray diffractometer, model 6000 at a scanning rate of 5 °C min^{-1}. Scanning electron microscopy images were obtained using a JEOL-7100F microscope and a Hitachi S4800, Japan. Transmission electron microscopy images were recorded using a JEM-2100F microscope as well as a JEOL F200 instrument equipped with EDS. XPS measurements were carried out using a VG Multi Lab 2000 instrument.

Electrochemical characterization: The electrochemical measurements of the NiCo-LDH/ACC electrodes were tested as a SC cathode and anode, respectively, in a three-electrode configuration using a CHI 760 E electrochemical workstation. A SCE, platinum foil (Pt) and a prepared NiCo-LDH/ACC electrode (1 cm^2) served as the reference electrode, counter electrode, and working electrode, respectively. The potentials were kept between 0 and 0.5 V versus SCE and −0.1-(−1.1) V versus SCE in 1 M KOH electrolyte.

Assembling full supercapacitor device: The symmetric SC device was fabricated using prepared NiCo-LDH/ACC electrodes as cathode and anode, respectively, in 1 M KOH electrolyte. Electrochemical impedance spectroscopy (EIS) was performed under a sinusoidal signal at open circuit potential over a frequency range from 0.01 to 10^5 Hz with a magnitude of 10 mV.

5. Calculations

Capacitance calculations from three-electrode system: The capacitances of the prepared electrodes were calculated from the galvanostatic charge/discharge curves using the equation shown below:

$$C = \frac{2\int I \cdot V(t)dt}{q \cdot \Delta V^2} \quad (6)$$

where C (F g^{-1}; F cm^{-2}) is the capacitance, I (A) is the discharge current, $V(t)$ is the discharge voltage excluding the IR drop, dt is the time differential, and q is mass loading, surface area or the volume of the electrode.

Capacitance calculation from two-electrode system: The capacitances of the fabricated SC device were calculated from galvanostatic charge/discharge curves, using the equation shown below:

$$C = \frac{2\int I \cdot V(t)dt}{q \cdot \Delta V^2}, \quad (7)$$

where C is the capacitance, I is the discharge current, $V(t)$ is the discharge voltage excluding the IR drop, dt is the time differential, q is mass loading on the surface area, and ΔV is the volume of the fabricated SC device.

The energy and power densities at different current densities were calculated using the equations below:

$$E = \frac{\int I \cdot V(t)dt}{3600q} \quad (8)$$

$$P = \frac{3600E}{\Delta t} \quad (9)$$

where E is energy density, P is power density, I is discharge current, $V(t)$ is the discharge voltage excluding the IR drop, dt is time differential, Δt is the discharge time, and q is the total mass loading.

Acknowledgements

X. C. acknowledges the funding from Natural Science Foundation of China (No. 52003163), Guangdong Basic and Applied Basic Research Foundation (No. 2022A1515010670), Science and Technology Innovation Commission of Shenzhen (Nos. KQTD20170810105439418 and 20200812112006001), and NTUT-SZU Joint Research Program (Nos. 2022005 and 2022015). He also appreciates the help from the electron microscopy center in Shenzhen University for testing of the aberration-corrected HAADF STEM.

Conflict of Interest

The authors declare no conflict of interest.

Supporting Information

Supporting Information is available from the Wiley Online Library or from the author.

Keywords

amorphous nanosheets, aqueous supercapacitor, high volumetric/areal energy density, NiCo-LDH, room temperature synthesis

Received: August 2, 2022
Revised: October 3, 2022
Published online: October 12, 2022

[1] J. García-Martínez, *Nanotechnology for the Energy Challenge*, Wiley-VCH Verlag GmbH & Co. KGaA, Weinheim, Germany **2013**.
[2] Y. Gogotsi, *Nature* **2014**, *509*, 568.
[3] S. Chu, A. Majumdar, *Nature* **2012**, *488*, 294.
[4] M. Winter, R. J. Brodd, *Chem. Rev.* **2004**, *104*, 4245.
[5] M. Armand, J.-M. Tarascon, *Nature* **2008**, *451*, 652.
[6] S. Wang, D. Liu, X. Cai, L. Zhang, Y. Liu, X. Qin, R. Zhao, X. Zeng, C. Han, C. Zhan, F. Kang, B. Li, *Nano Energy* **2021**, *90*, 106510.
[7] X. Zeng, D. Liu, S. Wang, S. Liu, X. Cai, L. Zhang, R. Zhao, B. Li, F. Kang, A. C. S. Appl, *Mater. Interfaces* **2020**, *12*, 37047.
[8] J. Ding, W. Hu, E. Paek, D. Mitlin, *Chem. Rev.* **2018**, *118*, 6457.
[9] Y. Shao, M. F. El-Kady, J. Sun, Y. Li, Q. Zhang, M. Zhu, H. Wang, B. Dunn, R. B. Kaner, *Chem. Rev.* **2018**, *118*, 9233.
[10] C. F. Liu, Y. C. Liu, T. Y. Yi, C. C. Hu, *Carbon* **2019**, *145*, 529.
[11] J. Chen, M. Chen, W. Zhou, X. Xu, B. Liu, W. Zhang, C. Wong, *ACS Nano* **2022**, *16*, 2461.
[12] N. Choudhary, C. Li, J. Moore, N. Nagaiah, L. Zhai, Y. Jung, J. Thomas, *Adv. Mater.* **2017**, *29*, 1605336.
[13] G. G. Amatucci, F. Badway, A. du Pasquier, T. Zheng, *J. Electrochem. Soc.* **2001**, *148*, A930.
[14] K. A. Owusu, L. Qu, J. Li, Z. Wang, K. Zhao, C. Yang, K. M. Hercule, C. Lin, C. Shi, Q. Wei, L. Zhou, L. Mai, *Nat. Commun.* **2017**, *8*, 14264.
[15] Y.-J. Gu, W. Wen, J.-M. Wu, *J. Power Sources* **2020**, *469*, 228425.
[16] N. Jabeen, A. Hussain, Q. Xia, S. Sun, J. Zhu, H. Xia, *Adv. Mater.* **2017**, *29*, 1700804.
[17] W. Su, F. Wu, L. Fang, J. Hu, L. Liu, T. Guan, X. Long, H. Luo, M. Zhou, *J. Alloys Compd.* **2019**, *799*, 15.
[18] K. Qin, L. Wang, S. Wen, L. Diao, P. Liu, J. Li, L. Ma, C. Shi, C. Zhong, W. Hu, E. Liu, N. Zhao, *J. Mater. Chem. A* **2018**, *6*, 8109.
[19] X. Han, J. Li, J. Lu, S. Luo, J. Wan, B. Li, C. Hu, X. Cheng, *Nano Energy* **2021**, *86*, 106079.
[20] Q. Li, Y. Xu, S. Zheng, X. Guo, H. Xue, H. Pang, *Small* **2018**, *14*, 1800426.
[21] P. Geng, L. Wang, M. Du, Y. Bai, W. Li, Y. Liu, S. Chen, P. Braunstein, Q. Xu, H. Pang, *Adv. Mater.* **2022**, *34*, 2107836.
[22] W. Li, X. Guo, P. Geng, M. Du, Q. Jing, X. Chen, G. Zhang, H. Li, Q. Xu, P. Braunstein, H. Pang, *Adv. Mater.* **2021**, *33*, 2105163.
[23] S. Zheng, Q. Li, H. Xue, H. Pang, Q. Xu, *Nat. Sci. Rev.* **2020**, *7*, 305.
[24] T. Wang, Z. Kou, S. Mu, J. Liu, D. He, I. S. Amiinu, W. Meng, K. Zhou, Z. Luo, S. Chaemchuen, F. Verpoort, *Adv. Funct. Mater.* **2018**, *28*, 1705048.
[25] J. Zhang, T. Zhang, D. Yu, K. Xiao, Y. Hong, *CrstEngComm* **2015**, *17*, 8212.
[26] T. Guan, L. Fang, L. Liu, F. Wu, Y. Lu, H. Luo, J. Hu, B. Hu, M. Zhou, *J. Alloys Compd.* **2019**, *799*, 521.
[27] Y. Guo, X. Hong, Y. Wang, Q. Li, J. Meng, R. Dai, X. Liu, L. He, L. Mai, *Adv. Funct. Mater.* **2019**, *29*, 1809004.
[28] X. Li, H. Wu, C. Guan, A. M. Elshahawy, Y. Dong, S. J. Pennycook, J. Wang, *Small* **2019**, *15*, 1803895.
[29] Y. Sun, H. Xu, X. Zhao, Z. Hui, C. Yu, L. Wang, J. Xue, Y. Zhao, R. Zhou, H. Dai, *J. Mater. Chem. B* **2019**, *7*, 6232.
[30] K. A. Owusu, Z. Wang, L. Qu, Z. Liu, J. A.-A. Mehrez, Q. Wei, L. Zhou, L. Mai, *Chin. Chem. Lett.* **2020**, *31*, 1620.
[31] N. S. McIntyre, M. G. Cook, *Anal. Chem.* **2002**, *47*, 2208.
[32] Z. Lv, Q. Zhong, Y. Bu, *Adv. Mater. Interfaces* **2018**, *5*, 1800438.
[33] B. Li, P. Gu, Y. Feng, G. Zhang, K. Huang, H. Xue, H. Pang, *Adv. Funct. Mater.* **2017**, *27*, 1605784.
[34] H. Liang, J. Lin, H. Jia, S. Chen, J. Qi, J. Cao, T. Lin, W. Fei, J. Feng, *J. Power Sources* **2018**, *378*, 248.
[35] J. Yang, C. Yu, C. Hu, M. Wang, S. Li, H. Huang, K. Bustillo, X. Han, C. Zhao, W. Guo, *Adv. Funct. Mater.* **2018**, *28*, 1803272.
[36] J. Yang, C. Yu, X. Fan, Z. Ling, J. Qiu, Y. Gogotsi, *J. Mater. Chem. A* **2013**, *1*, 1963.
[37] G. Yilmaz, K. M. Yam, C. Zhang, H. J. Fan, G. W. Ho, *Adv. Mater.* **2017**, *29*, 1606814.
[38] L. Gao, J. U. Surjadi, K. Cao, H. Zhang, P. Li, S. Xu, C. Jiang, J. Song, D. Sun, Y. Lu, A. C. S. Appl, *Mater. Interfaces* **2017**, *9*, 5409.
[39] F. Zhu, W. Liu, Y. Liu, W. Shi, *Chem. Eng. J.* **2020**, *383*, 123150.

[40] X. Wu, Y. Ru, Y. Bai, G. Zhang, Y. Shi, H. Pang, *Coord. Chem. Rev.* **2022**, *451*, 214260.
[41] J. Zhang, K. Xiao, T. Zhang, G. Qian, Y. Wang, Y. Feng, *Electrochim. Acta* **2017**, *226*, 113.
[42] Y. He, X. Zhang, J. Wang, Y. Sui, J. Qi, Z. Chen, P. Zhang, C. Chen, W. Liu, *Adv. Mater. Interfaces* **2021**, *8*, 2100642.
[43] Z. Jiang, Z. Li, Z. Qin, H. Sun, X. Jiao, D. Chen, *Nanoscale* **2013**, *5*, 11770.
[44] J. Wang, Y. Wei, J. Yu, *Appl. Clay Sci.* **2013**, *72*, 37.
[45] L. Wei, H. E. Karahan, S. Zhai, H. Liu, X. Chen, Z. Zhou, Y. Lei, Z. Liu, *Adv. Mater.* **2017**, *29*, 1701410.
[46] Y. Liu, Y. Wang, C. Shi, Y. Chen, D. Li, Z. He, C. Wang, L. Guo, J. Ma, *Carbon* **2020**, *165*, 129.
[47] Y. Liu, X. Teng, Y. Mi, Z. Chen, *J. Mater. Chem. A* **2017**, *5*, 24407.
[48] C. Guan, X. Liu, W. Ren, X. Li, C. Cheng, J. Wang, *Adv. Energy Mater.* **2017**, *7*, 1602391.
[49] J. H. Lee, H. J. Lee, S. Y. Lim, K. H. Chae, S. H. Park, K. Y. Chung, E. Deniz, J. W. Choi, *Adv. Funct. Mater.* **2017**, *27*, 1605225.
[50] H. Lindström, S. Södergren, A. Solbrand, H. Rensmo, J. Hjelm, A. Hagfeldt, S.-E. Lindquist, *J. Phys. Chem. B* **1997**, *101*, 7717.
[51] Y. Jiang, L. Zhang, H. Zhang, C. Zhang, S. Liu, *J. Power Sources* **2016**, *329*, 473.
[52] Z.-H. Huang, F.-F. Sun, M. Batmunkh, W.-H. Li, H. Li, Y. Sun, Q. Zhao, X. Liu, T.-Y. Ma, *J. Mater. Chem. A* **2019**, *7*, 11826.
[53] X. Zheng, H. Quan, X. Li, H. He, Q. Ye, X. Xu, F. Wang, *Nanoscale* **2016**, *8*, 17055.
[54] J. Xiao, L. Wan, S. Yang, F. Xiao, S. Wang, *Nano Lett.* **2014**, *14*, 831.
[55] L. Liu, L. Fang, F. Wu, J. Hu, S. Zhang, H. Luo, B. Hu, M. Zhou, *J. Alloys Compd.* **2020**, *824*, 153929.
[56] D. Su, Z. Tang, J. Xie, Z. Bian, J. Zhang, D. Yang, D. Zhang, J. Wang, Y. Liu, A. Yuan, *Appl. Surf. Sci.* **2019**, *469*, 487.
[57] D. Chen, H. Chen, X. Chang, P. Liu, Z. Zhao, J. Zhou, G. Xu, H. Lin, S. Han, *J. Alloys Compd.* **2017**, *729*, 866.
[58] A. D. Jagadale, G. Guan, X. Li, X. Du, X. Ma, X. Hao, A. Abudula, *J. Power Sources* **2016**, *306*, 526.
[59] X. Cai, X. Shen, L. Ma, Z. Ji, C. Xu, A. Yuan, *Chem. Eng. J.* **2015**, *268*, 251.
[60] J.-J. Zhou, Q. Li, C. Chen, Y.-L. Li, K. Tao, L. Han, *Chem. Eng. J.* **2018**, *350*, 551.
[61] X. Wang, F. Huang, F. Rong, P. He, R. Que, *J. Mater. Chem. A* **2019**, *7*, 12018.
[62] Y. Zhao, X. He, R. Chen, Q. Liu, J. Liu, J. Yu, J. Li, H. Zhang, H. Dong, M. Zhang, *Chem. Eng. J.* **2018**, *352*, 29.
[63] C. Xia, Q. Jiang, C. Zhao, P. M. Beaujuge, H. N. Alshareef, *Nano Energy* **2016**, *24*, 78.
[64] H. Li, Y. Gao, C. Wang, G. Yang, *Adv. Energy Mater.* **2015**, *5*, 1401767.
[65] J. Chen, H. Chen, M. Chen, W. Zhou, Q. Tian, C. P. Wong, *Chem. Eng. J.* **2022**, *428*, 131380.
[66] G. Nagaraju, S. C. Sekhar, B. Ramulu, J. S. Yu, *Small* **2019**, *15*, 1805418.
[67] W. Chen, T. Wei, L.-E. Mo, S. Wu, Z. Li, S. Chen, X. Zhang, L. Hu, *Chem. Eng. J.* **2020**, *400*, 125856.
[68] C. Chen, D. Yan, X. Luo, W. Gao, G. Huang, Z. Han, Y. Zeng, Z. Zhu, A. C. S. Appl, *Mater. Interfaces* **2018**, *10*, 4662.
[69] C. Chen, S. Wang, X. Luo, W. Gao, G. Huang, Y. Zeng, Z. Zhu, *J. Power Sources* **2019**, *409*, 112.
[70] S. Guan, X. Fu, Z. Lao, C. Jin, Z. Peng, *ACS Sustain. Chem. Eng.* **2019**, *7*, 11672.
[71] J. Hao, S. Peng, H. Li, S. Dang, T. Qin, Y. Wen, J. Huang, F. Ma, D. Gao, F. Li, *J. Mater. Chem. A* **2018**, *6*, 16094.